Calculating the *S*-matrix of low-energy heavy-ion collisions using quantum coupled-channels wave-packet dynamics

Terence Vockerodt and Alexis Diaz-Torres
Department of Physics, University of Surrey, Guildford GU2 7XH, United Kingdom

We investigate the fusion and scattering of a ^{16}O projectile on ^{152,154}Sm targets using the time-dependent coupled-channels wave-packet method. We benchmark calculations of the *S*-matrix elements, fusion cross sections, and scattering differential cross sections with those from the time-independent coupled-channels method, and compare the results to experimental data. We find that our time-dependent method and the time-independent method produce quantitatively similar results for the *S*-matrix elements and fusion cross sections, but our method cannot quantitatively explain the experimental scattering differential cross sections, mainly due to the low maximum number of partial waves produced by the time-dependent method. Nevertheless, the strong agreements between our method and the time-independent method demonstrates that the time-dependent coupled-channels wave-packet method can be used to address fusion reactions for a wide range of energies, with the advantage of being able to extend to time-dependent Hamiltonians for more advanced modeling of nuclear reactions.

I. INTRODUCTION

In nuclear reaction theory, there are a host of low-energy phenomena that are unable to be expressed simultaneously using many of the contemporary models. In low-energy nuclear reactions, there is an interplay between quantum and dynamical effects such as quantum tunneling and nuclear friction [1] that can enhance or hinder the formation of the compound nucleus. Classical attempts at describing nuclear friction such as solving the Langevin equation have not been categorically successful in describing low-energy observables [1–7], and there will always be ambiguity in the sources of errors due to the nonquantum nature of the Langevin equation.

It is very desirable to use fully quantum mechanical methods to describe these phenomena. Even in the few-body perspective, a nuclear reaction Hamiltonian that encompasses all scattering and fusion phenomena can be very involved, with many channel labels to consider such as mass asymmetry, elongation, angular momenta, as well as target and projectile spins [8]. These large basis sizes can prove difficult to perform global optimizations such as those used in time-independent methods in a timely manner, whereas time-dependent methods may be able to explore the parts of the Hilbert space most relevant to the reaction in less computation time. Specifically, if one wishes to treat internal radial and/or angular coordinates of the nuclei explicitly [9,10], or perform calculations using a heat bath [11], then time-dependent methods can explore these relatively large Hilbert spaces faster than time-independent methods. With the upcoming development of exciting technologies like zeptosecond laser pulses [12], which we hope can provide better state control of the fusing system, as well as the inability to model catastrophic astrophysical events with stellar nuclear plasma in the laboratory [13], there are a lot of

nuanced applications where it seems only time-dependent theoretical models can be used. For the latter application that we described, nuclear reactions in a stellar plasma environment can be modeled as an open quantum system, which falls under the class of time-dependent methods.

We find that the time-dependent coupled-channels wave-packet (TDCCWP) method is a promising path forward in performing calculations for heavy-ion systems. The TDC-CWP method is a few-coordinate method, which involves solving the two body time-dependent Schrödinger equation (TDSE) using a Chebyshev polynomial propagator [14]. The potentials used in the TDCCWP method can be built from microscopical, many body models, and the resulting time propagation is highly accurate [14]. In order to describe observables such as scattering differential cross sections, the TDCCWP method incorporates the use of energy projection methods, which provide us with results as if we propagated an energy eigenstate of the Hamiltonian of the collective radial motion, much like how nuclear reactions are performed in the laboratory.

Previously, we investigated the use of a window operator in order to resolve our initial and final states of the time propagation in energy with relative success [14]. However, we were concerned that for future applications of energy resolution that the window operator could have inaccurate results even with optimal parameters (since the window operator only approximates the energy projection). We were also concerned of the computation time needed to perform the necessary matrix inverses to calculate the energy resolution on the Fourier grid used. The Fourier grid that we need in order to properly propagate the TDSE is larger than typical grids used to solve the time-independent Schrödinger equation (TISE), and therefore the matrix inverses are very inefficient on the Fourier grid.

There have been methods developed in the field of quantum chemistry that calculate energy projection using integrations over the time coordinate [15], which have not been used yet to describe the types of nuclear systems we have mentioned above.

In the present work we perform a feasibility study of the TDCCWP method for ^{16}O + ^{152,154}Sm reactions, which is an extension of the work of the first author's Ph.D. thesis [16]. The main aim of this paper is to benchmark calculations of the S-matrix elements, fusion cross sections, and scattering differential cross sections to time-independent methods. The paper layout is as follows: Section II details all the nuclear theory equations that we will attempt to calculate. Section III features our results and discussion, where we calculate the S-matrix elements, fusion cross sections, and differential cross sections using the TDCCWP method, for the first time in the context of time-dependent quantum nuclear reaction theory. These results are benchmarked against results generated from time-independent methods, and compared with experimental data. Section IV contains our conclusions and some examples of future work to address problems in the method. The Appendix details our so called "curation procedure," which is used to extract more accurate and useful results from our raw data.

II. THEORY

A. Coupled-channels Hamiltonian

Consider a projectile nucleus of mass M_P and numbers Z_P, A_P, incident on a deformed target nucleus of mass M_T and numbers Z_T, A_T. We assume that the projectile is both spherical and inert, the target is initially in the ground state with spin zero, and that the target spin Hamiltonian is approximated by the rigid rotor model [8]. We express the TDSE for the relative motion in the isocentrifugal approximation [17,18], for target spin I_n channel wave function $\psi_{n,J}(r, t)$, as

$$i\hbar \frac{\partial \psi_{n,J}(r,t)}{\partial t} = \left(\frac{-\hbar^2}{2\mu} \frac{d^2}{dr^2} + \frac{J(J+1)\hbar^2}{2\mu r^2} + U(r) + iW(r) \right.$$
$$\left. + \frac{I_n(I_n+1)\hbar^2}{2\mathcal{I}} \right) \psi_{n,J}(r,t)$$
$$+ \sum_{n'} V_{nn'}(r)\psi_{n',J}(r,t), \quad (1)$$

where r is the inter-nuclear distance, $\mu = \frac{M_P M_T}{M_P + M_T}$ is the reduced mass of the target-projectile system, J is the total angular momentum, $U(r)$ is the nuclear radial potential, $W(r)$ is the radial absorption potential that accounts for fusion, $\mathcal{I}$ is the moment of inertia of the target, and $V_{nn'}(r)$ is the coupling potential between the rotational eigenstates of the target. The nuclear radial potential has the form

$$U(r) = -\frac{V_{WS}}{1 + \exp[(r - r_{WS})/a_{WS}]} + \frac{Z_P Z_T e^2}{r}, \quad (2)$$

where V_{WS} is the strength of the Woods-Saxon potential, $r_{WS} = r_{WS0}(A_P^{1/3} + A_T^{1/3})$ is the range of the Woods-Saxon potential, r_{WS0} is a constant radius parameter, a_{WS} is the diffuseness parameter, and $e^2 \approx 1.44$ MeV fm. The radial

absorption potential is expressed as

$$W(r) = -\frac{W_0}{1 + \exp[(r - r_{pock})/a_W]}, \quad (3)$$

where W_0 is the absorption well strength, a_W is the absorption potential diffuseness parameter, and r_{pock} is the location of the pocket of the nuclear potential, or the shortest distance where the nuclear potential in Eq. (2) is minimized.

B. Coupling matrix elements

The coupling potential is expressed as the sum of the nuclear and Coulomb couplings, given by [19]

$$V_{nn'}(r) = V_{N,nn'}(r) + V_{C,nn'}(r). \quad (4)$$

The effect of the target-projectile coupling is modeled as a deformation in the effective radius of the target, which modifies the unperturbed radius r_{WS} and thus modifies the Woods-Saxon potential [19]. We describe this deformation of the effective radius using the operator $\hat{r}_{def}$. The nuclear coupling is given by [19]

$$V_{N,nn'}(r) = \sum_{\zeta} \langle I_n | \zeta \rangle \langle \zeta | I_{n'} \rangle V_N(r, \lambda_\zeta) - V_N(r, 0)\delta_{nn'}, \quad (5)$$

where $\delta_{nn'}$ is the Kronecker delta, $\hat{r}_{def} |\zeta\rangle = \lambda_\zeta |\zeta\rangle$, and

$$V_N(r, \lambda_\zeta) = -\frac{V_{WS}}{1 + \exp[(r - r_{WS} - \lambda_\zeta)/a_{WS}]}. \quad (6)$$

The eigenstates $|\zeta\rangle$ are composed of the basis spin states $|I_n\rangle$, so we can find the states $|\zeta\rangle$ using the following matrix elements:

$$\langle I_n | \hat{r}_{def} | I_{n'} \rangle = r_T [\beta_2 \mathcal{F}(2, I_n, I_{n'}) + \beta_4 \mathcal{F}(4, I_n, I_{n'})], \quad (7)$$

where $r_T = r_{coup} A_T^{1/3}$, r_{coup} is the coupling radius parameter, β_2 and β_4 are the deformation parameters for the quadrupole and hexadecapole modes respectively, and

$$\mathcal{F}(I, I_n, I_{n'}) = \sqrt{\frac{(2I+1)(2I_n+1)(2I_{n'}+1)}{4\pi}} \begin{pmatrix} I_n & I & I_{n'} \\ 0 & 0 & 0 \end{pmatrix}^2, \quad (8)$$

where the bracketed array is a 3-j symbol. The Coulomb coupling potential is expressed as [19]

$$V_{C,nn'}(r) = \frac{3Z_P Z_T}{5} \frac{r_T^2}{r^3} \left(\beta_2 + \frac{2}{7}\sqrt{\frac{5}{\pi}} \beta_2^2 \right) \mathcal{F}(2, I_n, I_{n'})$$
$$+ \frac{3Z_P Z_T}{9} \frac{r_T^4}{r^5} \left(\beta_4 + \frac{9}{7\sqrt{\pi}} \beta_2^2 \right) \mathcal{F}(4, I_n, I_{n'}). \quad (9)$$

In the present work, we choose to use only the 0^+, 2^+, and 4^+ states in the target rotational band. This is because in this work our main objective is to benchmark the TDCCWP results to the time-independent methods, and a smaller than usual rotational band is necessary to reduce computation time for these tests. That being said, we show later on in Fig. 12 that for ^{154}Sm the introduction of new states in the rotational band does not drastically affect results such as the fusion cross sections, so this truncated basis does have applicability and relevance to some nuclear fusion observables.

C. Fusion/differential cross sections and *S*-matrix elements

In general, the scattering differential cross sections for final channel β given the entrance channel α are given by [20]

$$\frac{d\sigma_{\beta\alpha}(E, \theta, \phi)}{d\Omega} = \frac{v_\beta}{v_\alpha}|f_{\beta\alpha}(E, \theta, \phi)|^2, \qquad (10)$$

where E is the kinetic energy of the radial motion, $f_{\beta\alpha}(E, \theta, \phi)$ is the scattering amplitude, and v_γ is the velocity of flux in channel γ. For a beam that is initially aligned in the z direction [which leads to no ϕ dependence in Eq. (10)], the scattering amplitude for collisions involving charged particles in the isocentrifugal approximation is given by [20]

$$f_{\beta\alpha}(E, \theta) = f_C(\theta)\delta_{\alpha\beta} + \frac{1}{2ik_\alpha}\sqrt{\frac{v_\alpha}{v_\beta}}\sum_J (2J + 1)\exp(2i\sigma_{\alpha,J})$$
$$\times \left[S^{\mathrm{BF}}_{\beta\alpha}(E, J) - \delta_{\alpha\beta}\right]P_J[\cos(\theta)], \qquad (11)$$

where $f_C(\theta)$ is the Rutherford scattering amplitude, k_α is the wave number of the entrance channel α, $\sigma_{\alpha,J}$ are the Coulomb phase shifts, $S^{\mathrm{BF}}_{\beta\alpha}(E, J)$ are the body-fixed on-shell *S*-matrix elements, and $P_J[\cos(\theta)]$ are Legendre polynomials. The on-shell body-fixed *S*-matrix elements are expressed as [15]

$$S^{\mathrm{BF}}_{\beta\alpha}(E, J) = \langle \chi^+_{\beta,E,J} | \chi^-_{\alpha,E,J}\rangle, \qquad (12)$$

where $|\chi^\pm_{\gamma,E,J}\rangle$ are the energy resolved asymptotic states of the body-fixed Hamiltonian for excitation channel γ with angular momentum J, with the $+/-$ distinguishing between outgoing/ingoing radial states. Consider the initial state in entrance channel α for our time propagation $|\psi^-_{\alpha,J}(t_i)\rangle$, where t_i is the initial time, which is a superposition of ingoing body-fixed asymptotic states. We can extract the asymptotic state from the initial state using an energy projection operator

$$|\chi^-_{\alpha,E,J}\rangle = \frac{1}{\Lambda_{\alpha,E,J}}\delta(\hat{H} - E)|\psi^-_{\alpha,J}(t_i)\rangle, \qquad (13)$$

where

$$\Lambda_{\alpha,E,J} = \langle \chi^-_{\alpha,E,J} | \psi^-_{\alpha,J}(t_i)\rangle, \qquad (14)$$

and similarly for $|\chi^+_{\beta,E,J}\rangle$ via some outgoing final state $|\psi^+_{\beta,J}\rangle$. By expressing the energy projection as an integral over time, Eq. (12) can be expressed as [15]

$$S^{\mathrm{BF}}_{\beta\alpha}(E, J) = \frac{-1}{2\pi\hbar\Lambda^*_{\beta,E,J}\Lambda_{\alpha,E,J}}\int_{-\infty}^{\infty} dt \exp(\frac{iE(t - t_i)}{\hbar})$$
$$\times \langle\psi^+_{\beta,J}|\psi^-_{\alpha,J}(t)\rangle. \qquad (15)$$

We now present a novel choice of initial and final states that reduce the error in the calculation of the *S*-matrix elements significantly (compared to using the more standard Gaussian wave packets). This extent of the error reduction is shown in the results section of this work. We choose the final states $|\psi^+_{\beta,J}\rangle$ so that their radial wave functions are of the form

$$\langle r|\psi^+_{\beta,J}\rangle = \exp\left(\frac{-(r - r_f)^2}{2\sigma_f^2}\right) \times \langle r|\chi^+_{\beta,E_f,J}\rangle, \qquad (16)$$

where E_f is an arbitrarily chosen final energy, taken to be equal to E. Thus for the Hamiltonian in this work, the final radial wave functions are the outgoing energy resolved

asymptotic Coulomb wave-functions, modulated by a Gaussian envelope. The incident wave has a similar form,

$$\langle r|\psi^-_{\alpha,J}(t_i)\rangle = \exp\left(\frac{-(r - r_i)^2}{2\sigma_i^2}\right) \times \langle r|\chi^-_{\alpha,E_i,J}\rangle, \qquad (17)$$

where r_i is the center of the initial wave packet, σ_i is the radial width, and E_i is the initial energy. The Gaussian envelope function for both these choices of initial and final wave functions intends to converge the *S*-matrix elements calculated using Eq. (15). The transmission coefficients can be expressed as

$$\mathcal{T}_\alpha(E, J) = 1 - \mathcal{R}_\alpha(E, J)$$
$$= 1 - \sum_\beta \left|S^{\mathrm{BF}}_{\beta\alpha}(E, J)\right|^2. \qquad (18)$$

From the transmission coefficients, we can calculate the fusion cross sections $\sigma_{\mathrm{fus}}(E)$ using [20]

$$\sigma_{\mathrm{fus}}(E) = \frac{\pi\hbar^2}{2\mu E}\sum_J (2J + 1)\mathcal{T}_\alpha(E, J). \qquad (19)$$

D. Overlapping of energy resolved results

Much like our previous work [9,10,14], there is a dependence of the generated energy resolved results and the initial energy E_i of the propagated wave packet. This dependence is due to the fact that each wave packet is a distribution of energies. For an arbitrary wave packet, the generated results match closest to the TISE results (for Hamiltonians where they should match) for energies E close to E_i. The matching gets worse the further away E is from E_i, because the absolute size of the energy coefficients of the wave packet in these energy regions are too low for accurate numerical calculations. For the state $|\psi\rangle$, its energy coefficients are defined as $\langle\Phi_E|\psi\rangle$, where $\hat{H}|\Phi_E\rangle = E|\Phi_E\rangle$, and $\hat{H}$ is the Hamiltonian. The low-coefficient problem is avoidable for a wide range of energies close to the barrier, by varying E_i in a range of interest.

In the set of initial energies $\{E_i\}$, it is optimal to choose values of E_i where there is overlap in the results for adjacent E_i values, which occurs for energies E where the energy coefficients for both wave packets are high enough for numerical calculations to remain accurate. This extent of overlap can be controlled by adjusting the width parameter of the initial wave packet σ_i. There is better overlap between adjacent E_i values when σ_i is decreased in value.

III. RESULTS

In this section, we show results for $^{16}\mathrm{O} + ^{152,154}\mathrm{Sm}$ collisions. Since the procedures used to generate the results are the same for both collisions, the only results that we show of the $^{16}\mathrm{O} + ^{152}\mathrm{Sm}$ reaction are the fusion cross sections and scattering differential cross sections, and unless explicitly mentioned all results pertain to the $^{16}\mathrm{O} + ^{154}\mathrm{Sm}$ reaction.

The propagation parameters used, shown in Table I, are different to our previous work in Ref. [14]. We increase the number of grid points and reduce $r_{\max}$, in order to produce good convergence and smooth integrals when using the

TABLE I. Model parameters used for the Fourier grid and the initial and final wave packets.

Parameter	Value	Description
NGP	3200	No. of Fourier grid points
r_{max} (fm)	350	Maximum r
r_i (fm)	150	Initial wave-packet position
σ_i (fm)	3	Initial wave-packet width
r_f (fm)	120	Final wave-packet position
σ_f (fm)	10	Final wave-packet width

Coulomb wave functions. We exploit this necessarily higher radial grid density by decreasing the initial wave-packet width parameter σ_i, in order to produce better overlap between the results from adjacent E_i values. The final state width parameter σ_f is chosen to be large in order for the coefficients $\langle \Phi_E | \psi_{\beta,J}^+ \rangle$ to be large. The nuclear parameters used for both reactions are shown in Table II.

However, for these grid parameters we cannot calculate the integral in Eq. (15) directly. This is because when the propagated initial state is ingoing, the overlap $\langle \psi_{\beta,J}^+ | \psi_{\alpha,J}^-(t) \rangle$ is highly oscillatory over time. It should integrate to zero analytically (since the final states are outgoing only), but the grid parameters used are not able to calculate a zero measure due to the highly oscillatory integrand. Therefore, we choose to begin calculating the integral in equation (15) only after the propagated wave packet is outgoing. This is practically achieved by integrating when $\langle \hat{k} \rangle$ is positive. This is a necessary but insufficient condition for a wave packet in our system to be outgoing. There may be components of the wave that reflect off of the barrier earlier than others, and therefore those early reflected components may not be counted using this condition if they pass the final wave packets before $\langle \hat{k} \rangle$ is positive. Therefore, in order to prevent the issue of early

TABLE II. Model parameters pertaining to the coupled-channels Hamiltonian for the ^{16}O and ^{152,154}Sm collisions, assuming the projectile is spherical and inert and the target has a ground rotational band with 0^+, 2^+, and 4^+ states. For ^{16}O and ^{154}Sm: the parameters are obtained from [21]. For ^{16}O and ^{152}Sm: the Woods-Saxon well depth was chosen to produce the $J = 0$ barrier height of 59.53 MeV (the barrier height is from Ref. [22]). The other Woods-Saxon, imaginary potential β_4 and coupling radius parameters are from Ref. [23]. The β_2 and ϵ_2 parameters are from Ref. [24]. Parameter ϵ_2 is used to determine the moment of inertia.

Parameter	Value (^{154}Sm)	Value (^{152}Sm)
V_{WS} (MeV)	165	69.5
r_{WS0} (fm)	0.95	1.20
a_{WS} (fm)	1.05	0.65
W_0 (MeV)	50	30
a_W (fm)	0.3	0.4
ϵ_2 (keV)	82	121.7817
β_2	0.322	0.3064
β_4	0.027	0.037
r_{coup} (fm)	1.06	1.1
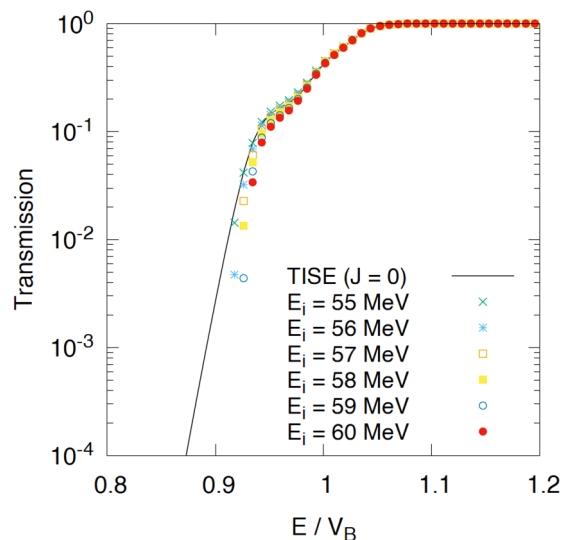
FIG. 1. Energy resolved transmission coefficients for varying mean incident wave-packet energy E_i and $J = 0$. Barrier height for $J = 0$ is equal to 59.41 MeV.

reflected momentum states from not being counted, we move the final wave functions to be sufficiently far away from the barrier.

A. Body fixed transmission coefficients and S-matrix elements

We begin by showing similar results to our previous work in Ref. [14]. In the present work, we use an overlapping procedure in order to reproduce the transmission coefficients from the CCFULL code [19], which are referred to from here on as the TISE transmission coefficients. We choose the set of E_i values to be six energy values that are 1 MeV apart, such that $\max(\{E_i\}) = \text{ceiling}[V_B(J)]$, where $V_B(J)$ is the height of the barrier from the combination of the Coulomb, nuclear, and centrifugal potentials. The high fidelity of the propagation that we reported in Ref. [14] is still maintained, despite the changes to the grid parameters. Figure 1 shows the calculations of the transmission coefficients using Eq (18) for $J = 0$ and our set of E_i values. For energies E above the barrier, there is a negligible dependence on E_i in the transmission coefficients, and they effectively are converged to unity. This is not the case with the window operator that we used in Ref. [14], which only had convergence of the above-barrier energies for mean incident wave-packet energies E_i high above the barrier. This presents an advantage for the S-matrix method over the window operator method: we can perform more propagations with mean incident wave-packet energies E_i below the barrier in order to better calculate and describe the nontrivial behavior for energies E below the barrier. This motivates our decision to use the set of E_i values that we mentioned earlier in this paragraph. We can see in Fig. 1 that adjacent E_i values produce transmission coefficients close in value to one another for all energies. Adjacent E_i values produce energy regions where the transmission coefficients are very close in value as expected. The details on how the S-matrix
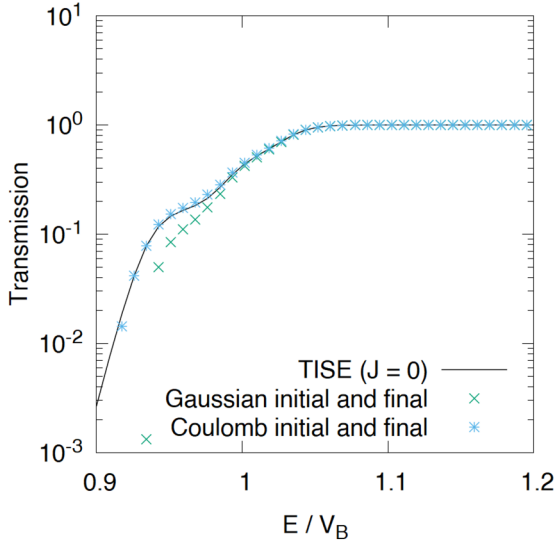
FIG. 2. Transmission coefficients for mean incident wave-packet energy $E_i = 55$ MeV for the two cases of initial and final wave functions explained in the text. Using two boosted Gaussian wave functions as in Ref. [14] provides poor matching of Eq. (18) to the TISE at below-barrier energies, while using two modulated Coulomb initial and final wave functions [Eqs. (17) and (16) respectively] provides significantly better matching.
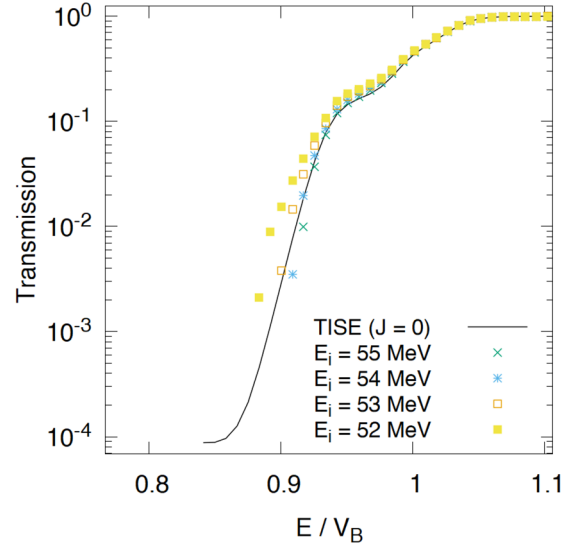

FIG. 3. Transmission coefficients for varying low mean incident wave-packet energy E_i. Propagating into lower E_i does not improve the matching of the TDCCWP transmission coefficients with the TISE.

elements/transmission coefficients are overlapped are in the Appendix.

We mentioned above that we use a novel choice of initial and final wave packets in order to reduce the error in the calculated results. This is demonstrated in Fig. 2, where we see that using two Gaussian wave packets (which are a Gaussian envelope boosted by a plane wave [14]) produces poor agreement to the TISE results. Using two Coulomb wave packets like our novel choices of Eqs. (17) and (16) produces much more accurate results. If one wishes to spend less computation time on time propagations in order to get a qualitative birds-eye view of the generated data quickly, then it is possible using Coulomb initial and final wave packets, which may be of immense practical advantage for testing new models in the early stages of development. This is not possible with the window operator method used previously, since it did not match nearly as well for a single energy and relied on the overlapping technique in order to correctly match the TISE.

While these results look promising, we need to go much deeper below the barrier in order to describe scattering correctly. This is because for any given energy E, there is a contribution to the scattering from many partial waves J where $E \ll V_B(J)$. We investigated the possibility of doing this by decreasing E_i further below the barrier. While the time propagations remained stable, the calculated results were not quantitatively accurate. This is shown in Fig. 3, where we can see that decreasing E_i further below the barrier does not improve the matching to the TISE results. There is some behavior in the S-matrix elements and transmission that we expect to see analytically as $E \to 0$. As $E \to 0$, the elastic reflection should tend to unity and the inelastic to zero. This behavior can be used to estimate the S-matrix elements at low

energies via extrapolation techniques. To investigate this, we looked at the elastic and inelastic reflection probabilities from the S-matrix elements for decreasing E_i, shown in Figs. 4 and 5 respectively. Here, qualitatively we see the pattern we expect, with the elastic and inelastic reflections increasing and decreasing respectively as $E \to 0$. For $E_i = 55$ MeV, we see an unphysical increase in both the elastic and inelastic

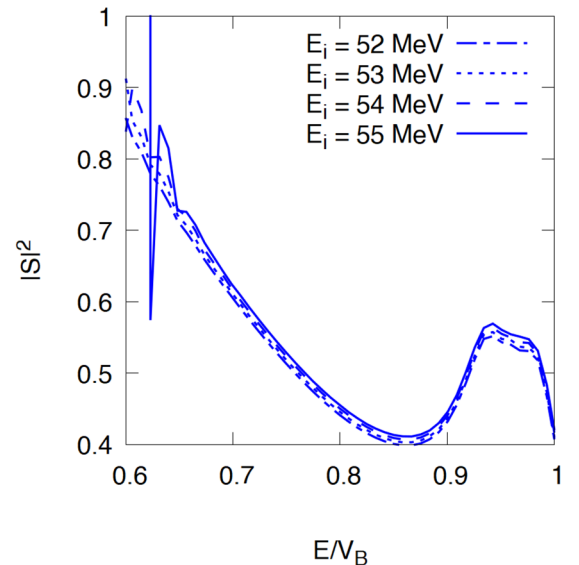FIG. 4. Reflection probabilities $|S_{\beta\alpha}^{\mathrm{BF}}(E, J)|^2$ for varying mean incident wave-packet energy E_i and final target spin state 0^+. The sign of the gradient is conserved as we decrease E_i, supporting the idea that this gradient stays negative, and brings the elastic S-matrix elements to unity as $E \to 0$. For decreasing E/V_B, each E_i value eventually generates a curve with unphysical results due to numerical inaccuracy.
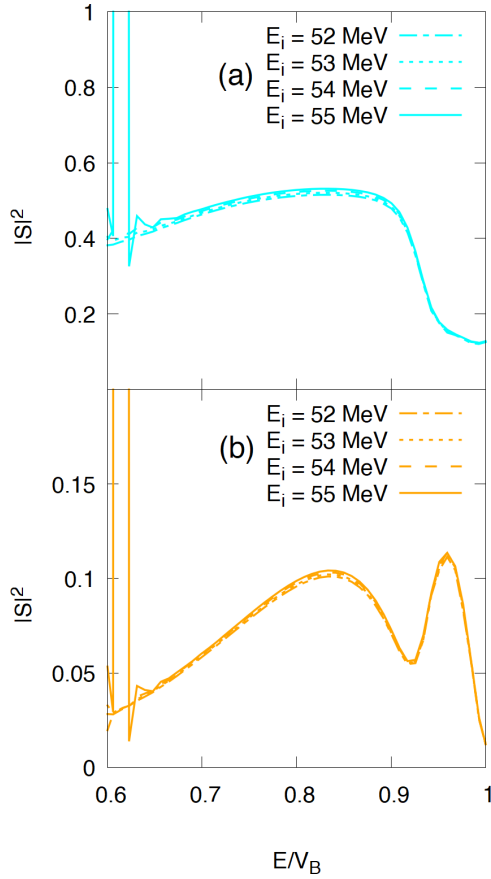
FIG. 5. Same as Fig. 4, but for (a) 2^+ and (b) 4^+ target rotational states. As mean incident wave-packet energy E_i is decreased, the sign of the gradient is positive and conserved, which will lead the inelastic S-matrix elements to zero as $E \to 0$.

reflections as $E \to 0$, due to numerical error (the $E_i = 55$ MeV wave-packet components at these low energies are very small, numerically speaking). Since the reflection probabilities qualitatively follow the trend we expect, we decided to use an extrapolation procedure detailed in the extrapolation section of the Appendix, on top of the overlapping procedure.

The curated transmission coefficients and reflection probabilities for $J = 0$ are shown in Figs. 6 and 7 respectively. We show a comparison to results from the TISE from two methods: the transmission coefficients are from the CCFULL code [19] and the reflection probabilities are from the FRESCO code on the isocentrifugal setting [25], as well as the scattering CCFULL code from Ref. [26]. Figure 6 shows an excellent agreement between the transmission results, and Fig. 7 shows similar but reasonable qualitative agreement between the three methods. The difference between the TDCCWP/CCFULL method and the FRESCO method is due to the inclusion of spin-orbit coupling factors in the calculation of the S-matrix elements in the FRESCO code, even in the isocentrifugal setting.

The phase angles of the S-matrix elements from the TD-CCWP method were also different from the FRESCO data (the FRESCO phase angles tend to zero as $E \to 0$ for the elastic channel, but the TDCCWP phase angles tended to a
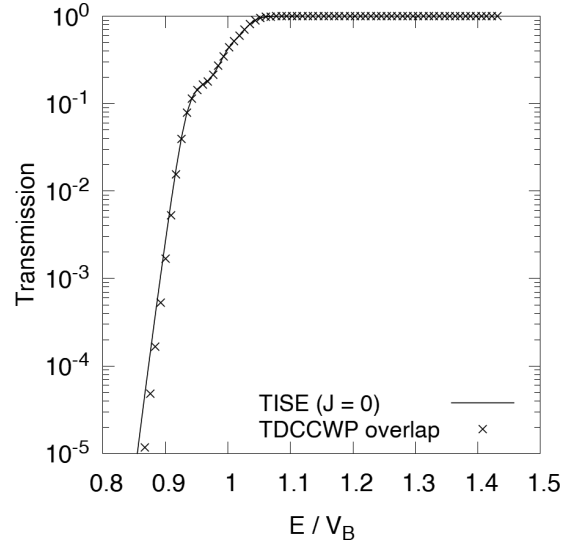

FIG. 6. Curated (overlapped and extrapolated) transmission coefficients. The overlapping procedure and logistic fitting procedures used in the curation process are described in the Appendix.

constant, nonzero value [16]). Since a nonzero phase angle in the low-energy elastic S-matrix elements prevents convergence of Eq. (11), we shifted the TDCCWP phases for all J by a constant phase angle in order to match the FRESCO results. This phase angle "fixing" is the final stage of the curation procedure of the TDCCWP method described in the Appendix. Figure 8 shows the curated phase shifts from this method for $J = 0$, which show good agreement with the FRESCO phase shifts for low energies. For high energies above the barrier, the TDCCWP phase angle becomes erratic, due to the numerical impossibility of calculating the phase of a fully transmitted (and thus absorbed) wave in our framework. However, since
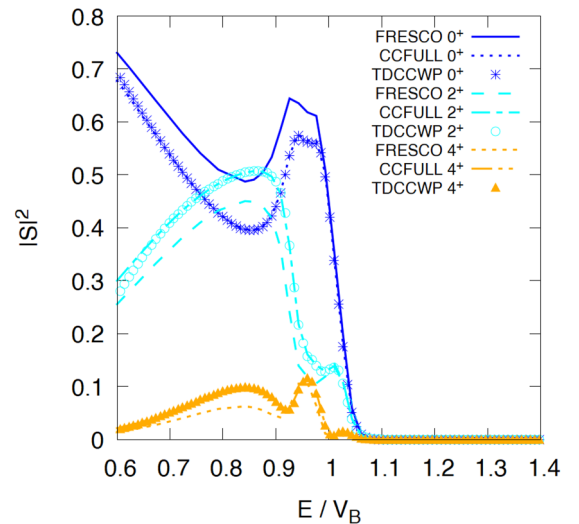

FIG. 7. Comparison between the TDCCWP, CCFULL, and FRESCO results for the reflection probabilities $|S_{\beta\alpha}^{\mathrm{BF}}(E, J)|^2$ for $J = 0$. Differences between the methods are detailed in the text. The results between all methods are qualitatively similar.
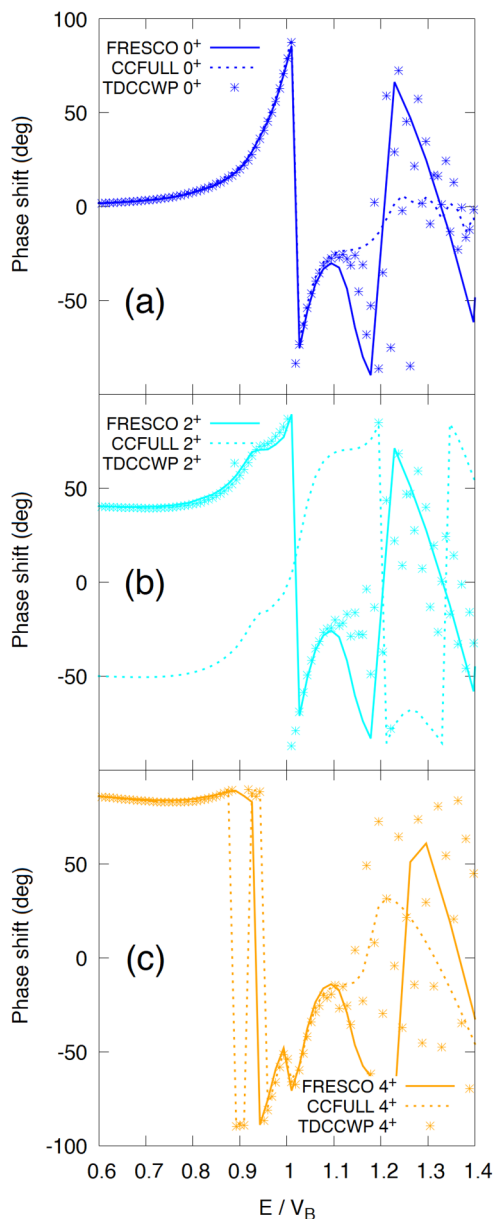
FIG. 8. Total (nuclear + Coulomb) phase shifts for $J = 0$ and the (a) 0^+, (b) 2^+, and (c) 4^+ target states. Phase shifts determined by dividing the phase of the S matrix by 2. The solid line is the FRESCO calculation and crosses are from the TDCCWP method after adding a constant phase. The constant phase was chosen to be the value such that the phase shifts for both methods are equal at $E = 35$ MeV.

the S-matrix elements tend to zero for high energies (relative to the barrier), the erratic phases do not affect the calculation of Eq. (11). The three methods produce similar results for all final states except for the 2^+ state, where the CCFULL results differ from the TDCCWP and FRESCO results. We will find that this phase shift difference is a constant, and therefore has no impact on the inelastic differential cross section results, since global phases in the S matrix in Eq. (11) are factored out when calculating the mod squared of the scattering amplitude for the inelastic case.
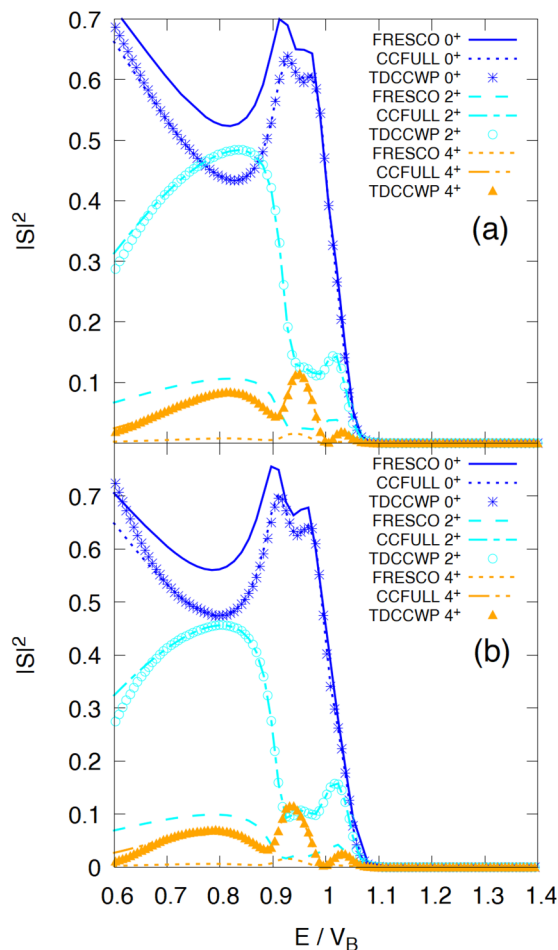

FIG. 9. Comparison between TDCCWP, CCFULL, and FRESCO S-matrix reflection probabilities for (a) $J = 20$ and (b) $J = 30$. Barrier height at $J = 20$ is 64.69 MeV, and at $J = 30$ is 71.38 MeV.

Figures 9 and 10 show the reflection probabilities and the phase shifts respectively for $J = 20,\ 30$, with similar agreement to what we saw between the TDCCWP and TISE methods for $J = 0$. For the elastic S-matrix elements for $J = 0,\ 20,\ 30$ in Figs. 8 and 10, we can see that a π phase shift occurs near $E = V_B(J)$, which is what we physically expect from the system. From Figs. 7 and 9, as J increases we can see the development of a local maximum in the interval $1 < E/V_B < 1.05$, and two local minima in the interval $0.9 < E/V_B < 1$ in the 2^+ reflection probability. Figures 7 and 9 also show a local maximum locating deeper below the barrier energy in the 4^+ reflection probability. These two effects coincide with one another and produce a situation where the 4^+ reflection probability is greater than the 2^+ reflection probability at $E \approx 66$ MeV. To verify this, we propagated a wave packet with $E_i = 66$ MeV and $J = 30$, and we see in Fig. 11 that the 4^+ scattering is at a similar order of magnitude to the 2^+ scattering. In Fig. 10, the π phase shift at $E \approx 0.9V_B$ for the 4^+ final state is no longer present in the TDCCWP phase, but is in the CCFULL phase. This is likely due to fixing the TDCCWP phase angles to the FRESCO $J = 0$ phase angles for all J, but
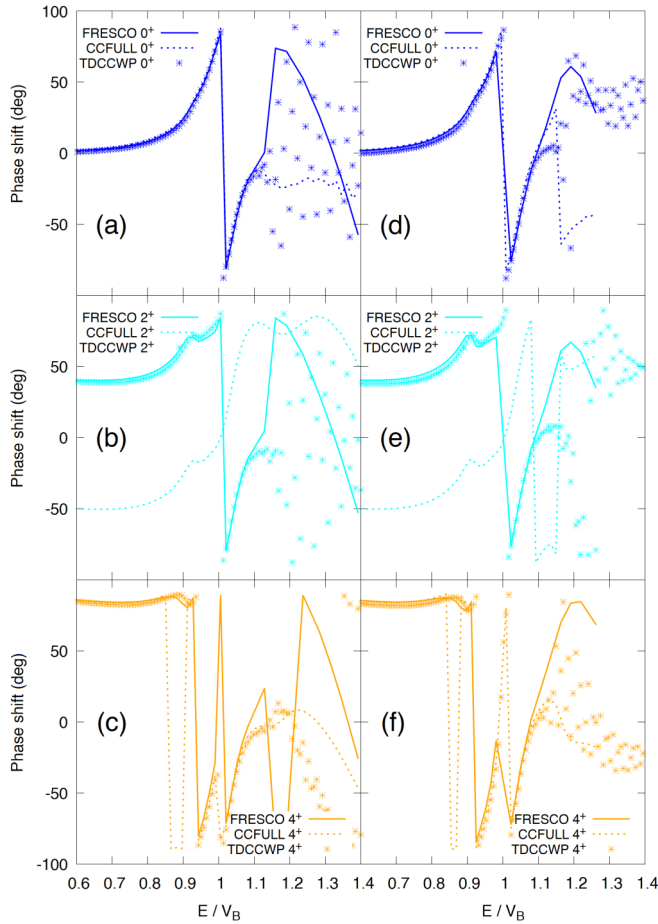
FIG. 10. Same as Fig. 8, but for the $J = 20$ and $J = 30$ phase shifts. Panels (a), (b), and (c) are the 0^+, 2^+, and 4^+ target state phase shifts respectively for $J = 20$, and panels (d), (e), and (f) are the 0^+, 2^+, and 4^+ target state phase shifts respectively for $J = 30$.

we show later in this work that this does not affect the results for the 4^+ differential cross sections. The strong quantitative similarities between the TDCCWP and CCFULL S-matrix elements and the TDCCWP and FRESCO phase shifts give us confidence that we can reasonably attempt a calculation of the differential cross sections and other observables.
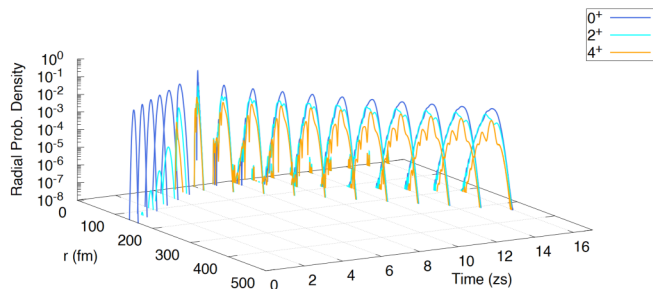

FIG. 11. Time propagation of a radial wave-packet for $E_i = 66$ MeV and $J = 30$, which illustrates the effect of the similar inelastic reflection probabilities at this energy from Fig. 9. The 0^+, 2^+, and 4^+ results are blue (dark grey), cyan (light grey), and orange (grey) respectively.
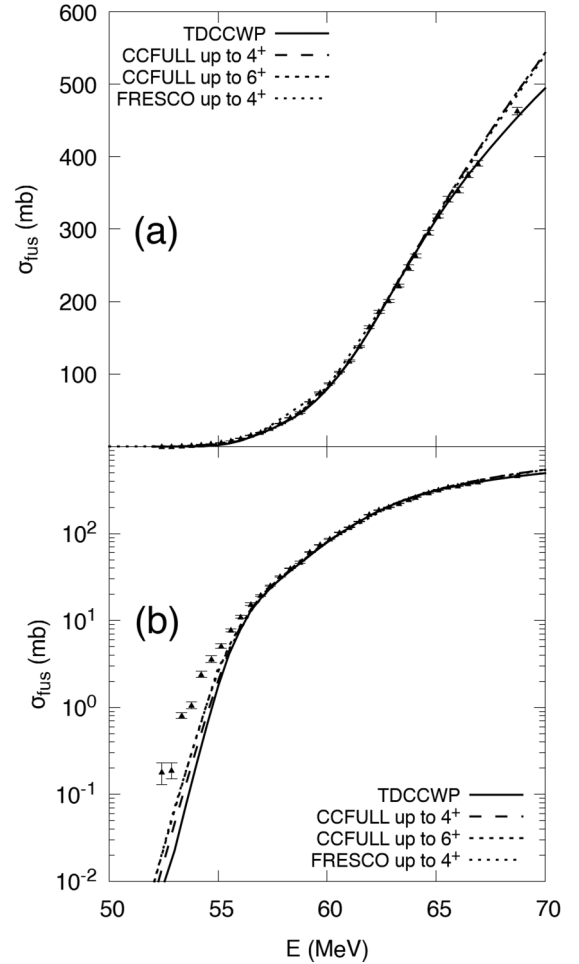

FIG. 12. Comparison to experimental data of the $^{16}O + ^{154}Sm$ fusion cross sections for the TDCCWP, CCFULL, and FRESCO models with (a) linear and (b) logarithmic scales. We include up to $J = 30$ partial waves in the TDCCWP results. We vary the number of channels in the CCFULL calculation. Adding more channels does not affect the fusion cross sections significantly. Experimental data are from Ref. [27].

B. Fusion cross sections and scattering differential cross sections

We will now compare the TDCCWP, CCFULL, and FRESCO fusion cross section and scattering differential cross sections to experimental data. Figure 12 shows the fusion cross sections, which have good agreement for all methods for energies near the $J = 0$ barrier height. The TDCCWP and CCFULL methods disagree for energies far below the $J = 0$ barrier due to the nature of our extrapolation, but the results are of a similar order of magnitude. Further below the $J = 0$ barrier, the experimental results show what is known as "fusion enhancement" [27]. This is expected because the theoretical models used in this work do not include multinucleon transfer reactions such as deep inelastic collisions in the Hamiltonian, which can account for the difference seen here.

Figure 13 shows the quasielastic scattering differential cross sections as a function of energy for $\theta = 175°$ for up to $J = 30$ partial waves for a $^{16}O + ^{154}Sm$ collision and up to $J = 45$ partial waves for a $^{16}O + ^{152}Sm$ collision. Partial
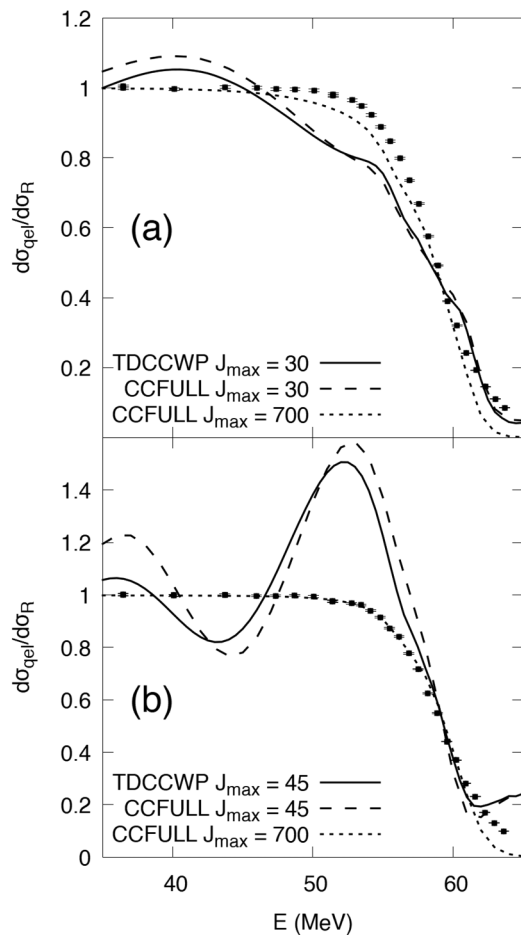
FIG. 13. Comparison to experimental data of the quasielastic scattering of (a) $^{16}O + ^{154}Sm$ and (b) $^{16}O + ^{152}Sm$ for $\theta = 175°$ for partial waves up to (a) $J = 30$ and (b) $J = 45$. Converged CCFULL results for $J = 700$ are also shown. Experimental data are from Refs. [22] and [28] for $^{16}O + ^{154}Sm$ and $^{16}O + ^{152}Sm$ respectively.

waves up to $J = 30$, which are sufficient to describe near barrier fusion for these nuclei, are insufficient for describing scattering differential cross sections in general. Therefore, we increased the number of partial waves generated when we modeled the $^{16}O + ^{152}Sm$ collision. Going further than $J = 45$ produces numerical errors in the curation procedure, since the gradients like those in Figs. 4 and 5 are no longer negative and positive respectively, but completely flat. This makes extrapolation of the same quality and consistency of those for lower J values impossible. Figure 13(a) shows good qualitative agreement between the TDCCWP and CCFULL data sets for energies close to the $J = 0$ barrier height, but not enough partial waves to replicate the experimental data. Figure 13(b) shows similar agreement, but the similarity is weaker due to the extrapolation methods used for the TDC-CWP results. As J is increased, the difference between the TDCCWP and CCFULL S-matrix elements is greater for energies in the extrapolation region (compare Figs. 7 and 9, and Figs. 8 and 10 for instance), which manifests itself in Fig. 13. Despite this, the agreement is still reasonable, but a more sophisticated extrapolation procedure is desired for describing
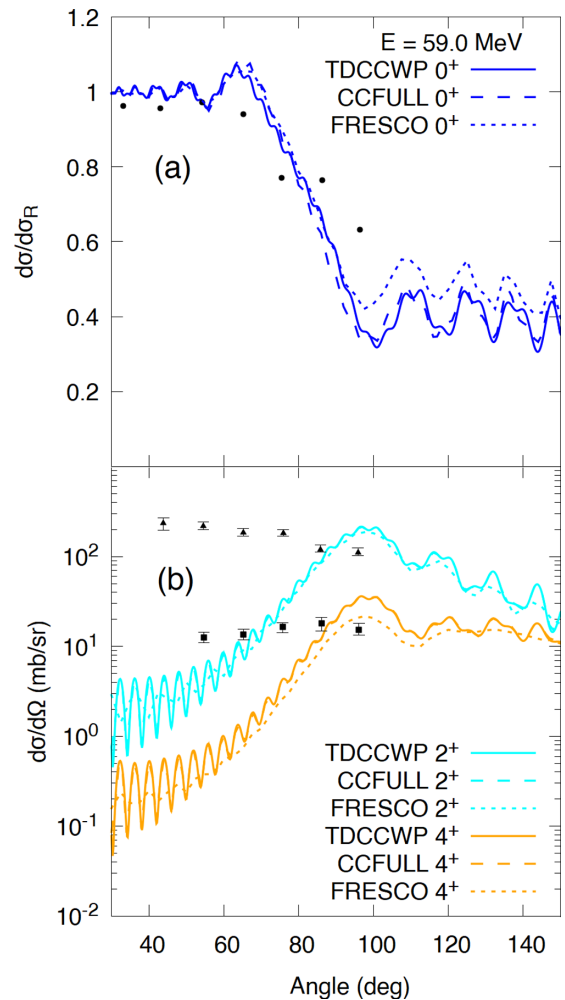

FIG. 14. TDCCWP and FRESCO (a) elastic and (b) inelastic differential cross section calculations compared to the scattering experimental data for $^{16}O + ^{152}Sm$. The computational results were generated by summing partial waves up to $J = 45$. Experimental 0^+ data are from Ref. [29], and the 2^+ (triangles) and 4^+ (squares) data are from Ref. [30]. In panel (b), 2^+ and 4^+ results are cyan (light grey, upper) and orange (grey, lower) respectively.

very low-energy phenomena. We have included the converged CCFULL curves for the fusion cross sections, which includes partial waves up to $J = 700$. This is not currently achievable with the TDCCWP method, since as mentioned previously the present method only works up to $J = 45$. The converged CC-FULL curve is in good agreement with the experimental data for $^{16}O + ^{152}Sm$, meaning that the TDCCWP method can be a good predictor of experimental data, subject to concentrated improvement on its weaknesses in predicting low-energy and high-J S-matrix elements.

Despite the low number of partial waves able to be generated, we show a comparison between the TDCCWP, CCFULL, FRESCO, and experimental scattering differential cross sections for a $^{16}O + ^{152}Sm$ collision at $E = 59$ MeV in Fig. 14. We see near perfect quantitative agreement between the TDCCWP and CCFULL inelastic scattering differential cross sections, despite the phase shift differences in Figs. 8

and 10. We see qualitative agreement between the TDCCWP and FRESCO scattering differential cross sections in both the elastic and inelastic cases. However, no data set agrees with the experimental data for up to $J = 45$ partial waves. While the inelastic TDCCWP and CCFULL scattering differential cross sections follow each other near perfectly, the elastic scattering differs slightly, likely due to slight differences between the phase angles, courtesy of the angle fixing in our curation procedure. This is because the angle fixing shifts the S-matrix phases so that they match the phase of the $J = 0$ FRESCO S matrix at $E = 35$ MeV, but there is a slight J dependence on the FRESCO and CCFULL S-matrix phases (compare Figs. 8 and 10). Nevertheless, in Fig. 14 the agreement is very strong between the TDCCWP and CCFULL method results, indicating a successful benchmark of the scattering differential cross sections.

We wonder what the TDCCWP results might look like if the method could produce results at high numbers of partial waves. Therefore, we show the fully converged CCFULL and FRESCO scattering differential cross sections and the experimental data for a $^{16}O + ^{152}Sm$ collision at $E = 59$ MeV in Fig. 15. The convergence required partial waves up to $J = 700$, which as mentioned before is not currently feasible with the TDCCWP method. There is a reasonable agreement between the experimental and FRESCO scattering differential cross sections, although interestingly there is not a solid agreement between the elastic scattering differential cross sections for both methods at forwards angles. The calculations did not include excited states in the target higher than the 4^+ state in ^{152}Sm, which could account for the difference in the scattering. Notably, the FRESCO results are closer to the experimental curves, which suggests that the use of spin-orbit coupling is a solid approach for accurately calculating the experimental values. Ultimately, given the quantitative/qualitative similarities between the TDCCWP and CCFULL/FRESCO method results, we expect that the TDCCWP method with the isocentrifugal approximation relaxed can produce similar results to the experimental data, provided of course that a sufficient number of partial waves can be generated.

IV. CONCLUSIONS

By using novel choices of initial states and optimized grid parameters, we were able to generate transmission coefficients and S-matrix elements for a wide range of energies, including some below barrier. The energy range where we could generate good results was deemed insufficient for describing scattering differential cross sections, and propagating wave-packets with lower and lower initial energies was providing unphysical results. Therefore, we employed a curation procedure that used extrapolation techniques in order to describe the transmission and S-matrix elements for $E \rightarrow 0$. This produced quantitatively/qualitatively similar results to the time-independent coupled-channels method implemented in the CCFULL/FRESCO code. Only a qualitative agreement with the FRESCO results was expected since FRESCO uses a different treatment of the isocentrifugal approximation to the TDCCWP method. More crucially, despite the simple nature
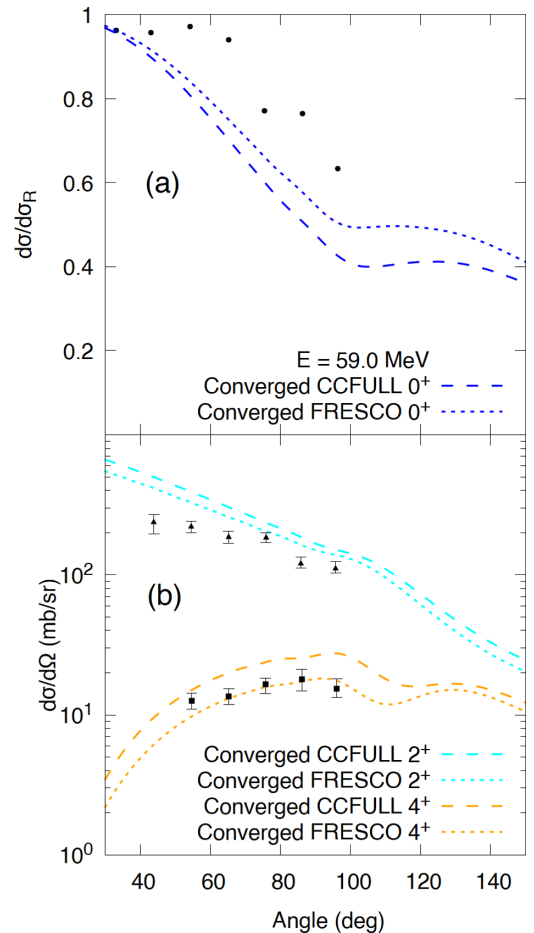

FIG. 15. Converged CCFULL and FRESCO (a) elastic and (b) inelastic differential cross section calculations and the experimental data. The computational results were generated by summing partial waves up to $J = 700$. Experimental 0^+ data are from Ref. [29], and the 2^+ (triangles) and 4^+ (squares) data are from Ref. [30]. In panel (b), 2^+ and 4^+ results are cyan (light grey, upper) and orange (grey, lower) respectively.

of the extrapolation methods in the curation procedure, the TDCCWP results are a similar order of magnitude to the CCFULL results. The CCFULL results are a much better benchmark for the performance of the TDCCWP method in the present work, due to both methods using the same treatment of the Hamiltonian. For such a simple extrapolation procedure, the TDCCWP can produce a good approximation of the CCFULL results for a wide range of energies. More sophisticated methods can be implemented in the curation procedure in order to extrapolate the S-matrix elements, some of which we discuss in more detail below.

When comparing the TDCCWP results to the experimental data for $^{16}O + ^{152,154}Sm$, we found an expected quantitative disagreement due to the lack of partial waves in the evaluation of the scattering differential cross sections. The isocentrifugal approximation is also expected to impact the result, but is less crucial in terms of the disagreement. While the isocentrifugal approximation can be relaxed in the Hamiltonian relatively easily [31,32], generating results using the TDCCWP method

for high J partial waves is not possible using the proposed method in this work. This is because the curation procedure fails to produce accurate results for $J > 45$.

We have a few suggestions to remedy this obvious problem, which depend on the system we wish to study. If the time-dependent effects that we are simulating have a trivial characteristic in the results for all J values, then we suggest using the TDCCWP method alongside a time-independent method such as that implemented in CCFULL or FRESCO in order to generate high J value partial waves. The TDCCWP method will be used solely to determine the quantitative nature of the time-dependent effects on the results, which is then applied to the time-independent results as a correction. However, if the time-dependent effects do not produce a consistent and trivial characteristic in the results, then we suggest using an artificial neural network (ANN) [33] to attempt to learn the patterns in the S-matrix elements with varying J. The features (inputs) that should be given to the ANN are properties of the barrier such as barrier height, width, and position, as well as the energies E. For the output layer, the ANN should try and learn the S-matrix elements. A useful aspect of this method is that training data for the neural network can be provided at sparse J values, and the ANN can either interpolate to intermediate J values, extrapolate to higher J values, or both. This may be able to save a lot computation time.

However, even if an ANN can be used to learn the patterns of our curated S-matrix elements across different J values, a more systematic approach to determining low-energy S-matrix elements is greatly desirable. It would be interesting to see what happens both mechanistically from the time propagation, as well as what kinds of characteristics appear in the S-matrix elements at low energies, such as resonances. A strong and well documented computational approach will be useful here in order to calculate the integrals of small numbers. Simulating low-energy reactions using the TDCCWP method requires a longer overall reaction time, so wave packets with minimal to no spreading/diffusion such as those from the Airy functions [34] may be useful to investigate this problem.

We expect that the TDCCWP method can be readily used to describe fusion cross sections for time-dependent Hamiltonians without much further work, since the fusion cross sections converge for smaller J values which are easier to generate from the TDCCWP method. Overall, the TDCCWP method performed well when benchmarked against the CCFULL scattering method, and can be of great interest to time-dependent problems in nuclear theory; subject to a proper and more rigorous treatment of the low-energy and high angular momenta S-matrix elements.

APPENDIX: TDCCWP CURATION PROCEDURE

As mentioned in the text, the curation procedure is a combination of overlapping the S-matrix elements, extrapolating the S-matrix elements to low energies, and fixing the phase shifts.

1. Overlapping

We find that, in order to best reproduce the results from the TISE, one uses the S-matrix elements/transmission coefficients of the first E_i value for energies up to 0.5 MeV above E_i, the second E_i for energies 0–1 MeV above E_i, the third E_i for energies 0.5–1.5 MeV above E_i, the forth E_i for energies 1–2 MeV above E_i, the fifth E_i for energies 1.5–2.5 MeV above E_i and the sixth E_i for energies 2 MeV above E_i. This produces the same quality of convergence demonstrated in Fig. 6 for all J values.

2. Extrapolation

Given what we know about the low-energy limits of the complex radii of the S-matrix elements $|S_{\beta\alpha}^{\mathrm{BF}}(E, J)|$ and Figs. 4 and 5, the behavior of the sub-barrier complex radii of the S-matrix elements appears similar to the logistic function. We can express the low-energy complex radii as

$$\left|S_{\beta\alpha}^{\mathrm{BF}}(E, J)\right| = \frac{\left|S_{\beta\alpha}^{\mathrm{BF}}(E, J)\right|_{\mathrm{sigmax}}}{1 + \exp[-\beta(E - E_{\mathrm{mid}})]} + C, \qquad (A1)$$

where $|S_{\beta\alpha}^{\mathrm{BF}}(E, J)|_{\mathrm{sigmax}}$ is the maximum value of the sigmoid part of the complex radii within the extrapolation region, β is the steepness, E_{mid} fixes the midpoint of the curve, and C is a constant. Assuming $\beta > 0$ and $C = 0$, for $E \ll E_{\mathrm{mid}}$ the curve plateaus at zero, and for $E \gg E_{\mathrm{mid}}$ it plateaus at $|S_{\beta\alpha}^{\mathrm{BF}}(E, J)|_{\mathrm{sigmax}}$. This behavior is qualitatively similar to what we expect from both our S-matrix complex radii and the transmission coefficients, and thus this choice of fitting function is sensible. For simplicity, both the transmission coefficients and the S-matrix elements are extrapolated into low energies using a logistic function, but the resulting S-matrix elements are normalized using the new transmission coefficients. The transmission coefficients were extrapolated using the generated values of the transmission values in the energy range $[\min(E_i) - 0.5, \min(E_i) + 1]$, and the S-matrix elements were extrapolated using the generated values in the energy range $[0.7V_B(J), 0.8V_B(J)]$. To assist the sigmoid fitting for the S-matrix elements, we fit using extra reflection probabilities for energies up to 3 MeV, set to 1 if we are fitting the elastic S-matrix elements and 0 for the inelastic.

3. Angle fixing

The angle fixing procedure involves several parts. First, the numerically generated results do not explain the low energies well, and have errors in the phase shifts that seem to originate from the low-energy errors in Figs. 4 and 5. The complex phase angles of the S-matrix elements $\Phi_{\beta\alpha}(E, J)$ are extrapolated using a Taylor expansion using the lowest E_i data set,

i.e.,

$$\Phi_{\beta\alpha}(E, J) = \sum_{n=0}^{n_{max}} \frac{\Phi_{\beta\alpha}^{(n)}(E_{ex}, J)}{n!} (E - E_{ex})^n, \quad (A2)$$

where E_{ex} is a low energy taken to be $0.7V_B(J)$ and $\Phi_{\beta\alpha}^{(n)}(E_{ex}, J)$ is the nth order derivative of $\Phi_{\beta\alpha}(E, J)$ evaluated at E_{ex}, which is approximated using a central finite difference method,

$$\Phi_{\beta\alpha}^{(n)}(E_{ex}, J) = \frac{\Phi_{\beta\alpha}^{(n-1)}(E_{ex} + \Delta E, J) - \Phi_{\beta\alpha}^{(n-1)}(E_{ex} - \Delta E, J)}{2\Delta E},$$

$$(A3)$$

where $\Delta E = 0.5$ MeV, which is the spacing of our energy grid. The $\Phi_{\beta\alpha}^{(n-1)}(E_{ex} \pm \Delta E, J)$ are evaluated using backwards and forwards finite difference methods respectively. To ensure accuracy, n_{max} was chosen to be equal to 50. The entire phase shift profile is then shifted by a constant phase angle. We shift the angles such that the TDCCWP phase angles at $E = 35$ MeV match the FRESCO phase angles at $E = 35$ MeV for $J = 0$. For $^{16}O + ^{154}Sm$, the low-energy FRESCO phase angles are 3.16°, 81.17°, and 172.75° for the 0^+, 2^+, and 4^+ phase angles respectively. For $^{16}O + ^{152}Sm$, the low-energy FRESCO phase angles are 3.88°, 81.23°, and 174.91° for the 0^+, 2^+, and 4^+ phase angles respectively.

[1] R. W. Hasse, Rep. Prog. Phys. **41**, 1027 (1978).

[2] A. Fukushima, A. Nasirov, Y. Aritomo, T. Wada, and M. Ohta, in *Tours Symposium on Nuclear Physics VI*, 5–8 September 2006, Tours, France, edited by M. Arnould, M. Lewitowicz, H. Emling, H. Akimune, M. Ohta, H. Utsunomiya, T. Wada, and T. Yamagata, AIP Conf. Proc. No. 891 (AIP, New York, 2007), p. 443.

[3] Y. Abe, A. Marchix, C. Shen, B. Yilmaz, G. Kosenko, D. Boilley, and B. G. Giraud, Int. J. Mod. Phys. E **16**, 491 (2007).

[4] Y. Aritomo, Prog. Theor. Phys. Suppl. **146**, 503 (2002).

[5] D. Gross and H. Kalinowski, Phys. Rep. **45**, 175 (1978).

[6] H. Hofmann, Phys. Rep. **284**, 137 (1997).

[7] P. Fröbrich and I. Gontchar, Phys. Rep. **292**, 131 (1998).

[8] W. Greiner and J. A. Maruhn, *Nuclear Models* (Springer-Verlag, Berlin, 1997).

[9] M. Boselli and A. Diaz-Torres, Phys. Rev. C **92**, 044610 (2015).

[10] A. Diaz-Torres and M. Wiescher, Phys. Rev. C **97**, 055802 (2018).

[11] M. Tokieda and K. Hagino, Ann. Phys. (NY) **412**, 168005 (2020).

[12] Extreme Light Infrastructure—nuclear physics, available at https://eli-laser.eu/, accessed 02/08/2021.

[13] E. B. Norman and D. N. Schramm, Astrophys. J. **228**, 881 (1979).

[14] T. Vockerodt and A. Diaz-Torres, Phys. Rev. C **100**, 034606 (2019).

[15] J. Dai and J. Z. H. Zhang, J. Phys. Chem. **100**, 6898 (1996).

[16] T. Vockerodt, Ph.D. thesis, University of Surrey, 2021 (unpublished), doi: https://doi.org/10.15126/thesis.900012.

[17] A. B. Balantekin and N. Takigawa, Rev. Mod. Phys. **70**, 77 (1998).

[18] K. Hagino and N. Takigawa, Prog. Theor. Phys. **128**, 1061 (2012).

[19] K. Hagino, N. Rowley, and A. T. Kruppa, Comput. Phys. Commun. **123**, 143 (1999).

[20] G. R. Satchler, *Introduction to Nuclear Reactions* (Palgrave Macmillan, London, 1990).

[21] A. Diaz-Torres, G. G. Adamian, V. V. Sargsyan, and N. V. Antonenko, Phys. Lett. B **739**, 348 (2014).

[22] C. J. Lin, H. M. Jia, H. Q. Zhang, F. Yang, X. X. Xu, F. Jia, Z. H. Liu, and K. Hagino, Phys. Rev. C **79**, 064603 (2009).

[23] H. Zhang, C. J. Lin, H. M. Jia, L. Yang, X. X. Xu, F. Yang, Z. D. Wu, Z. H. Liu, N. R. Ma, L. J. Sun *et al.*, EPJ Web Conf. **117**, 04010 (2016).

[24] S. Raman, J. C. W. Nestor, and P. Tikkanen, At. Data Nucl. Data Tables **78**, 44 (2001).

[25] I. J. Thompson, Comput. Phys. Rep. **7**, 167 (1988).

[26] K. Hagino, N. Rowley, and A. Kruppa, CCFULL: A program for quasi-elastic scattering, available at http://www2.yukawa.kyoto-u.ac.jp/~kouichi.hagino/ccfull.html, accessed 17/09/2021.

[27] J. R. Leigh, M. Dasgupta, D. J. Hinde, J. C. Mein, C. R. Morton, R. C. Lemmon, J. P. Lestone, J. O. Newton, H. Timmers, J. X. Wei, and N. Rowley, Phys. Rev. C **52**, 3151 (1995).

[28] H. M. Jia, C. J. Lin, F. Yang, X. X. Xu, H. Q. Zhang, Z. H. Liu, Z. D. Wu, L. Yang, N. R. Ma, P. F. Bao, and L.J. Sun, Phys. Rev. C **90**, 031601(R) (2014).

[29] P. Talon, N. Alamanos, M. Lamehi-Rachti, C. Levi, and L. Papineau, Nucl. Phys. A **359**, 493 (1981).

[30] T. Izumoto, T. Udagawa, and B. T. Kim, Phys. Rev. C **51**, 761 (1995).

[31] R. T. Pack, J. Chem. Phys. **60**, 633 (1974).

[32] Y. Sun, R. S. Judson, and D. J. Kouri, J. Chem. Phys. **90**, 241 (1989).

[33] I. Nunes and H. S. da Silva, *Artificial Neural Networks: A Practical Course* (Springer, Cham, 2018).

[34] M. V. Berry and N. L. Balazs, Am. J. Phys. **47**, 264 (1979).